Research Article

Pulvinar Slits: Cellulose-deficient and De-esterified Homogalacturonan-rich Structures in a Legume Motor Cell

Masahiro Takahara[1*], Satoru Tsugawa[2,3], Shingo Sakamoto[4,5],
Taku Demura[2,6], Miyuki T Nakata[2,6*†]
[*]These authors contributed equally.
[†]For correspondence. E-mail: mtn.plant@bs.naist.jp

[1]Acacia Horticulture, Kizugawa, Kyoto, Japan
[2]Graduate School of Science and Technology, Nara Institute of Science and Technology (NAIST), Ikoma, Nara, Japan
[3]Department of Mechanical Engineering, Faculty of Systems Science and Technology, Akita Prefectural University, Akita, Japan
[4]Plant Gene Regulation Research Group, Bioproduction Research Institute, National Institute of Advanced Industrial Science and Technology (AIST), Tsukuba, Japan
[5]Global Zero Emission Research Center, National Institute of Advanced Industrial Science and Technology (AIST), Tsukuba, Japan
[6]Center for Digital Green-innovation, Nara Institute of Science and Technology (NAIST), Ikoma, Nara, Japan

Short running title

Pulvinar Slits in a Legume Motor Cell

Affiliations

Acacia Horticulture, Kizugawa, Kyoto, Japan

Masahiro Takahara

Graduate School of Science and Technology, Nara Institute of Science and Technology (NAIST), Ikoma, Nara, Japan

Department of Mechanical Engineering, Faculty of Systems Science and Technology, Akita Prefectural University, Akita, 015-0055, Japan

Satoru Tsugawa

Plant Gene Regulation Research Group, Bioproduction Research Institute, National Institute of Advanced Industrial Science and Technology (AIST), Tsukuba, Japan

Global Zero Emission Research Center, National Institute of Advanced Industrial Science and Technology (AIST), Tsukuba, Japan

Shingo Sakamoto

Graduate School of Science and Technology, Nara Institute of Science and Technology (NAIST), Ikoma, Nara, Japan

Center for Digital Green-innovation, Nara Institute of Science and Technology (NAIST), Ikoma, Nara, Japan

Taku Demura, Miyuki T Nakata

Corresponding author

Miyuki T Nakata

Nara Institute of Science and Technology

Graduate School of Science and Technology

Division of Biological Science

8916-5 Takayama, Ikoma, NARA 630-0192 JAPAN

E-mail: mtn.plant@bs.naist.jp

Abstract

The cortical motor cells (CMCs) in a legume pulvinus execute the reversible deformation in leaf movement that is driven by changes in turgor pressure. In contrast to the underlying osmotic regulation, the cell wall structure of CMCs that contributes to the movement has yet to be characterized in detail. Here, we report that the cell wall of CMCs has tangential slits with low levels of cellulose deposition. This structure is unique and distinct from any other primary cell wall reported so far; thus, we named them "pulvinar slits." Notably, we predominantly detected de-methyl esterified homogalacturonan inside pulvinar slits, with a low deposition of highly methyl-esterified homogalacturonan inside the slits, as with cellulose. In addition, Fourier-transform infrared spectroscopy analysis indicated that the cell wall composition of pulvini is different from that of other axial organs, i.e. petioles or stems. Moreover, monosaccharide analysis showed that pulvini are pectin-rich organs like developing stems. Computer modeling suggested that pulvinar slits facilitate anisotropic extension in the direction perpendicular to the slits in the presence of turgor pressure. Mechanical tests revealed that the proximo-distal extensibility of pulvini is superior to that of the other axial organs. In this study, we thus established the distinctive cell wall structure of CMCs that contribute to plant movement, adding new knowledge to the structural diversity and function of the plant cell wall.

Abbreviations

CMC, a cortical motor cell; FTIR, Fourier-transform infrared spectroscopy; PCW, primary cell wall; SCW, secondary cell wall; HG, homogalacturonan; PD, proximo-distal; CBM3a, a carbohydrate-binding module 3; FEM, the finite-element method; PME, pectin methylesterases.

Introduction

A legume pulvinus is a joint-like thickening at the base of a leaf, leaflet, or rachis that plays a central role in leaf movement. Pulvinus-actuated leaf movements include circadian rhythm-driven movements completed over the scale of hours (Darwin and Darwin, 1880), blue light-induced movements in minutes (Koller, 1990), and touch-stimulated movements of Mimosoideae in seconds (Weintraub, 1952). During movement, a pulvinus is repeatedly and reversibly deformed by changing cell volume due to variation in the osmotic gradient. These repetitive and reversible steps are a unique feature that distinguish pulvinus-based movements from other types of organ movement driven by irreversible growth or by mechanical instability (Dumais and Forterre, 2012; Geitmann, 2016).

In general, osmotic gradients between the inside and the outside of a cell trigger directional water transport resulting in a change in cell volume. Cells swell when exposed to a hypotonic solution, while they contract in a hypertonic solution. Importantly, excessive expansion or contraction is blocked by the physical scaffold provided by the cell wall. When the cell volume increases in a hypotonic solution, cell walls act as a load-bearing structure against tensile stress. Therefore, the time derivative of cell volume depends on turgor pressure or cell wall extensibility under variable osmotic conditions, unless plasmolysis occurs (Geitmann and Ortega, 2009). In growing cells, cell walls are weak enough to yield under turgor, yet strong enough to offer mechanical resistance against bursting (Smithers et al., 2019).

The importance of the cell wall has been thoroughly investigated during the irreversible extension of growing cells (Cosgrove, 2005). Growing cells are surrounded by a primary cell wall (PCW) consisting mainly of cellulose, xyloglucan, and pectin, and they lack a secondary cell wall (SCW). Among PCW components, multiple cellulose polymers are bundled into microscale fibers, namely, cellulose microfibrils, to provide tensile stiffness and strength to the PCW. In axially expanding cells, the orientation of cellulose microfibrils often exhibits a bias perpendicular to the direction of expansion. In addition, xyloglucan and pectin contribute to cell wall extensibility by interacting with cellulose microfibrils (Cosgrove, 2005; Smithers et al., 2019). Xyloglucan crosslinks the hydrophobic segments of cellulose microfibrils to form a complex network, while pectin is a component of the matrix that fills the space between cellulose microfibrils by binding to their hydrophilic fraction (Cosgrove, 2005; Geitmann and Ortega, 2009; Zheng et al., 2018; Cosgrove, 2018). Thus, how the orientation, deposition, and structure of the cellulose microfibril network control cell wall extensibility and irreversible growth is well established and supported.

Unlike organ movement due to irreversible growth, pulvinus-driven movements are independent from growth (Darwin and Darwin, 1880). The pulvinus is comprised of several mature tissues, including the epidermis, cortical motor cells (CMCs), and vascular tissues (Fleurat-Lessard and Bonnenmain, 1978; Fleurat-Lessard and Roblin, 1982; Moysset and Simon, 1991). CMCs have a central role in the reversible deformation of the pulvinus. The CMCs that shrink when the pulvinus flexes are called extensor motor cells, while CMCs on the opposite side are called flexor cells. In the

early 1900s, changes in turgor of CMCs were proposed to be critical for leaf movements (Weintraub, 1952). Later, studies using runner bean (*Phaseolus coccineus*) reported anisotropic extension to the proximo-distal (PD) direction in an intact pulvinus during nyctinastic movement and in slices of CMCs exposed to different concentrations of mannitol (Mayer et al., 1985). Based on an estimation of the bulk moduli of extensibility of CMCs, this work concluded that the osmotic concentration in the apoplast determines by how much the CMC volume will change and actuate leaf movement. Therefore, the changes in osmotic concentration of CMCs have received much recent attention in various legume species with pulvini (Moran, 2007).

In this study, we focused on the structure of the CMC cell wall, which is not well characterized in contrast to the osmotic regulation of CMCs. Cellulose microfibrils are "tangentially" aligned in the cell wall of *P. coccineus* CMCs (Mayer et al., 1985); that is, they are aligned perpendicular to the PD axis. Indeed, the orientation of cellulose microfibrils appears to be consistent with the extension anisotropy of slices of CMCs as described above. However, the shape of each CMC does not show the same bias relative to the orientation perpendicular to that of cellulose microfibrils as seen in the case of irreversible growth. In addition, the orientation of cellulose microfibrils is closely associated with a slow irreversible extension referred to as "creep," but it is unclear whether the orientation alone is sufficient to explain the relatively rapid and reversible deformation of CMCs during leaf movement. In this study, we investigated the cell wall structure of CMCs in detail and discovered a hitherto undescribed slit-like structure that we designated pulvinar slits. Computational simulations suggested that the presence of pulvinar slits promotes extension in the PD direction, which we tested empirically by performing a mechanical test to compare the extensibility in the PD direction in pulvini with pulvinar slits and other axial organs lacking the slits. Our data suggest that the function of pulvinar slits is associated with PD extensibility and mechanical reversibility of CMCs.

Results

CMCs have tangential slits with less cellulose

To identify the cell wall structure of CMCs, we stained pulvini with calcofluor white, which stains cell wall components such as cellulose, in longitudinal and cross sections using pulvini freshly harvested from panicled-leaf ticktrefoil (*Desmodium paniculatum*), belonging to the Papilionoideae family (Figure 1A-F). Notably, in CMC longitudinal sections, we observed several slits with no significant fluorescence when stained by calcofluor white that run "tangentially" (Figure 1C, G). In vertical sections, we noticed small spots with no staining but no slits (Figure 1D, G). To determine whether tangential slits are specific to CMCs, we repeated the staining protocol on cortical cells collected from the boundary between a pulvinus and a petiole and from a longitudinal section of a petiole (Figure 1E, F). In both cases, we visualized small spots lacking staining but did not see tangential slits (Figure 1E, F). Since we only observed these tangential slits in pulvinus CMCs, we

149 designated the tangential slits as “pulvinar slits.”
150 To investigate the extent of conservation of pulvinar slits among legumes, we stained longitudinal
151 sections of pulvini from various legume species with calcofluor white. The Fabaceae family comprises
152 two major subfamilies: the Papilionoideae and the Caesalpinioideae (Azani et al., 2017). Importantly,
153 we detected slit structures in pulvinar CMCs from all 12 species selected and tested from these two
154 subfamilies (Supplemental Table 1, Figure 1H). In addition, we observed pulvinar slits in both adaxial
155 and abaxial pulvinar CMCs (Supplemental Figure 1). To make sure that the slits were not artifacts
156 arising during sectioning, we performed whole-mount staining. Again, we clearly observed slits in
157 CMCs from whole-mount-stained samples, with the slits located at the cell periphery (Figure 1I). We
158 therefore concluded that pulvinar slits are an innate cell wall structure of CMCs.
159 To validate the observation that a pulvinar slit is a region with lower cellulose deposition than its
160 surrounding region, we used cellulose-specific dyes, namely, pontamine and immunolabeling with an
161 antibody against type A carbohydrate-binding module 3 (CBM3a). With pontamine staining, we
162 detected tangential slits similar to those seen with calcofluor white staining in pulvinar CMCs (Figure
163 2A). Immunolabeling with CBM3a predominantly stains crystalline cellulose as speckles, but we also
164 found slit-like structures with lower signals (Figure 2B). Double staining with CBM3a and calcofluor
165 white indicates that slits lacking the CBM3a signal were colocalized with pulvinar slits, the structures
166 unstained by calcofluor white (Figure 2B, arrowheads). These observations indicated that pulvinar
167 slits are regions characterized by an extremely low cellulose deposition.
168 Taken together, we concluded that pulvinar slits are a structure specifically formed on the PCW of
169 CMCs, they have less cellulose than the surrounding cell wall, and they are widely conserved among
170 legume species.
171
172 **De-methyl esterification of homogalacturonan is associated with pulvinar slits**
173 To further characterize pulvinar slits, we examined the spatial pattern of other major PCW
174 components by immuno-histological analysis. Homogalacturonan (HG) is the most abundant pectin
175 and xyloglucan is the main hemicellulose detected in the PCW. HG is methyl-esterified during its
176 biosynthesis and later de-methyl-esterified during maturation. We detected a strong signal with the
177 LM19 antibody, which labels de-methyl-esterified HG, inside pulvinar slits with a stronger signal
178 close to the boundary with the rest of the PCW (Figure 3A, B). By contrast, the LM20 antibody, which
179 labels highly methyl-esterified HG, showed no signal in pulvinar slits (Figure 3A, C). We also labeled
180 XXXG-type xyloglucan with the LM15 antibody, which revealed dispersed signals throughout CMCs
181 (Figure 3A). We detected a faint signal with the 2F4 antibody, which labels calcium-crosslinked de-
182 methyl-esterified HG, although the signal appeared to be excluded from pulvinar slits (Supplemental
183 Figure 2A). We observed no signal when sections were incubated only with the secondary antibody
184 (Supplemental Figure 2B). These results thus suggested that de-methyl esterification of

homogalacturonan, probably without calcium cross-linking, is associated with pulvinar slits.

To better assess the composition of the pulvinus cell wall, we used Fourier-transform infrared spectroscopy (FTIR) and monosaccharide analysis to compare the cell wall from pulvini to that of other axial organs. Using the absorbance profile from FTIR, we identified several peaks (e.g. 778, 1317 cm^{-1}) and a range of 1620–1550 cm^{-1} that are specific to pulvini (Figure 4A). A principal component analysis revealed that the cell wall properties obtained from FTIR can be classified into three groups (shown as the dashed circles in Figure 4B), with pulvinar organs forming a group distinct from all of other axial organs (Figure 4B). The monosaccharide composition of pulvinar organs (primary pulvinus and secondary pulvinus) was also analyzed in detail. The xylose content mainly related to xylan in secondary cell wall of pulvini and developing stems was lower than that of petioles and mature stems (Figure 4C, Table 1). In contrast, pectin-related monosaccharides, such as galactose, arabinose, rhamnose and galacturonic acid were more abundant in pulvini (Figure 4C, Table 1). Especially, the abundance of galacturonic acid of pulvini was superior to developing stems (Figure 4C). Therefore, these results suggest that, despite being mature organs, pulvini have pectin-rich cell wall and resemble developing stems rather than mature organs (petioles and mature stems).

Pulvinar slits in the cell wall have a potential effect on the PD extensibility of pulvini

To explore the mechanical role of pulvinar slits in the turgor-triggered morphological changes of CMCs, we implemented the finite-element method (FEM) to determine how cell shape might be affected by the slits under turgor pressure. A previous study using a single cell layer sheet of onion (*Allium cepa*) peels indicated that cellulose mainly contributes to in-plane rigidity and plasticity, while pectin contributed very little (Zhang et al., 2019). Therefore, we hypothesized that pulvinar slits would present a mechanical defect when CMCs deform under turgor. We modeled CMCs as a hexagonal cell with several elliptical holes (Figure 5A). To set an accurate slit size for simulations, we measured cell length and the length and width of the slits in 59 randomly selected slits from eight species, yielding slit lengths ranging from 2.03 to 10.06 μm and a slit width from 0.32 to 2.26 μm. With a cell length of 20.6-46.1 μm, slit length was between 7.2% and 25.4% of overall cell length, with a mean of about 15%, while slit width was between 0.9% and 9.9% of cell length, with a mean of 3% (Figure 5B). We also calculated the slit index (length/width), which was 2.46–16.60 with a mean of about 6.14.

Based on these numbers as a standard slit property, we generated several cell models with different slit properties (Figure 5C-I). Using FEM, we simulated cell deformation under an isotropic pressure and analyzed the final cell shape. In this calculation, we evaluated the principal direction of growth of each triangle demonstrated in Figure 5C, representing a vertical elongation by blue and a horizontal elongation by red and in-between by white. With this setting, we can capture the local direction of growth by color diagram (Figure 5D, F, H). We explored the cell growth anisotropy as functions of slit shapes (Figure 5E), slit lengths (Figure 5G) and slit numbers (Figure 5I), respectively. These

221 simulations revealed that higher slit anisotropy, larger number of slits and larger slit area enhanced a
222 horizontal cell elongation. This result indicated that the slit structure promotes cell expansion in the
223 direction perpendicular to the slit. Pulvinar slits aligned in the tangential direction thus have a potential
224 effect on anisotropic cell extension to the PD direction upon turgor pressure.

225 The predictions by computer modeling were consistent with a previous finding that the extension of
226 *P. coccineus* pulvini shows a bias in the PD direction of the cell (Mayer et al., 1985). To confirm that
227 pulvini facilitate extensibility along the PD axis, we performed a compression test. In a uniaxial
228 compression test, a material generally expands in directions perpendicular to the direction of
229 compression, which is called the Poisson's effect. Using this principle, the continuous deformation in
230 the PD direction was recorded while compressing axial organs of *D. paniculatum* from a direction
231 perpendicular to the PD axis (Supplemental Figure S3A, B), and compared the PD extensibility of
232 pulvini with other axial organs. In addition, because pulvini are thought to be homologous to petiole-
233 like organs, petiolules, based on the *petiolule-like pulvinus* mutant phenotype in barrel clover
234 (*Medicago truncatula*) (Zhou et al., 2012), we also performed the compression test especially on
235 pulvini and petioles using samples from three other species. In *D. paniculatum*, we detected load
236 oscillation between approximately 0.4 and 0.6 of strain (equivalent to a reduction in height from the
237 original height to 40% and 60%, respectively) in almost all tested pulvini (Supplemental Figure S4A).
238 This load oscillation was similar to oscillation seen in stress-strain curve during brittle breaking under
239 compression. We observed a load oscillation in developing stems between approximately 0.3 and 0.8
240 of strain, but not in petioles and rarely in mature stems (Supplemental Figure S4A). The length of
241 pulvini along the PD axis slowly increased until the strain reached 0.3 but extended much more for
242 strain values above 0.4 (Figure 6A). The length of developing stems increased, but not as much as that
243 of pulvini (Figure 6A). We did not observe a statistically significant extension of petioles, while mature
244 stems only slightly extended under greater strain (Figure 6A). For a strain value of 0.5, the extension
245 rate of pulvini was higher than that of other axial organs (Figure 6B). Similarly, we determined that
246 pulvini display load oscillation and substantial PD extension in three other legume species, for a strain
247 value of 0.4 (Figure 6C, Supplemental Figure S4B, C). These results support the idea that pulvini have
248 excellent PD extensibility in comparison to other axial organs.

249 To test whether pulvinus extensibility is due to the PD extension of CMCs, we characterized the
250 deformation of pulvini. There were many tiny wrinkles aligned perpendicularly to the PD axis on the
251 pulvinar surface (Figure 6D, Supplemental Figure S3B, S5A), which gradually stretched along with
252 the PD extension during compression (Figure 6D, Supplemental Figure S3B). This phenomenon
253 resembled that previously reported during the leaf movements of *Mimosa pudica* (Song et al., 2014).
254 In cross-sectional views, CMCs became separated from the vascular bundles after compression
255 (Supplemental Figure S5B, C). These results indicate that the PD extension of a pulvinus by
256 compression results from the extension of CMCs and the spreading of tiny wrinkles in the epidermis,

together with the separation of CMCs and the vascular bundle (Supplemental Figure S5D).

Discussion

The pulvinus is a specialized organ that facilitates dynamic leaf movement. Here, we discovered that CMCs have a unique cell wall structure, designated the pulvinar slit, with a very low content of cellulose or highly methyl-esterified HG while being rich in de-methyl-esterified HG. In addition, we employed computational simulations to predict that the slits bestow CMCs with extensibility in the perpendicular direction. Finally, we demonstrated that the pulvinus has superior PD extensibility when compared to other axial organs. We summarize below the properties of the cell wall and speculate on the mechanical and physiological roles of pulvinar slits. We also discuss the similarities and differences between unique cell wall structures seen in pulvini and in other tissues. Finally, we place the discovery of pulvinar slits in context for a greater understanding of plant movement and cell wall mechanics.

We identified pulvinar slits as tangential slits after calcofluor white staining and established that the slits are widely conserved in legume species. Whole-mount staining revealed that the structures are not technical artifacts during sectioning but *bona fide* structures. Staining with pontamine and CBM3a lent support to our hypothesis that pulvinar slits reflect the pattern of cellulose deposition. De-methyl-esterified HG, probably without calcium crosslinking, appeared to accumulate abundantly inside pulvinar slits. By contrast, both cellulose and highly esterified HG were excluded from the pulvinar slits. FTIR analysis and monosaccharide analysis emphasized the distinct cell wall properties of pulvini relative to other axial organs and suggested the abundant deposition of pectin in pulvini. Mayer et al. showed that cellulose microfibrils are oriented “tangentially” (Mayer et al., 1985). Observations of pulvinar ultrastructure by transmission electron microscopy identified curving walls and pits including plasmodesmata on CMCs in transverse sections (Fleurat-Lessard and Roblin, 1988; Machado and Rodrigues, 2004; Rodrigues and Machado, 2006). We also observed similar pits here. Longitudinal sections of pulvini from *G. max* and *M. truncatula* were previously observed by microscopy after staining with toluidine blue O (Gao et al., 2017; Du et al., 2020), which visualizes various components of the cell wall including pectin (O'Brien et al., 1964; Mitra and Loqué, 2014). However, none of these earlier studies observed the slit-like structures, nor did they report on variation in cell wall thickness. The de-methyl-esterification of HG by pectin methylesterases (PMEs) was recently reported to enhance wall hydration and to increase cell wall thickness (Wang et al., 2020). Taken together, we propose that de-methyl-esterified HG has a role in thickening the cell wall within the slit, which accumulates little cellulose.

To explore the potential mechanical role played by pulvinar slits in turgor-triggered extension of CMCs, we performed a FEM simulation based on the assumption that the slits have a mechanical effect in a specific direction. The FEM results suggested that pulvinar slits have a potential effect on

293 anisotropic cell extension in the PD direction when the cell is under turgor pressure. This indicates
294 that the cell can control the mobility or reversible extensibility only by modifying the shape and size
295 of the slits structure. In this context, the shape anisotropy, number and size of the slits might be
296 meaningful because they determine the degree of how the cell deforms and deforms back. In a future
297 work, it should be a target to detect the correlations of the shape anisotropy, number and size of the
298 slits with a flexibility or bending property of the pulvini.
299 Previous studies using onion epidermal cells suggested that de-methyl-esterification of HG by PME
300 treatment causes increased in-plane plasticity of the cell wall but does not affect cell wall creep (Wang
301 et al., 2020). In addition, pectin enhances the strength of the cell wall perpendicular to the plane (Zhang
302 et al., 2019; Wang et al., 2020). However, the addition of calcium blocks the increase of plasticity
303 imparted by PME (Wang et al., 2020). Taken together, we propose that filling the slit with de-methyl-
304 esterified HG without calcium crosslinking achieves both in-plane plasticity and cell wall integrity. In
305 our experiments, we detected a faint signal with the 2F4 antibody (recognizing calcium cross-linked
306 HG) that did not appear to be associated with pulvinar slits. As calcium density in the cell wall can
307 change during leaf movement (Moysset et al., 2019), further analyses will be required to determine
308 whether the subcellular localization of calcium has an effect on the mechanical properties of the slits,
309 including a mechanical test at the cellular level.
310 In terms of a physiological role, pulvinar slits may also regulate turgor pressure. Pits observed in
311 previous studies in cross sections were proposed to contribute to volume changes of CMCs and to be
312 related to water transport, like xylem cell pits (Machado and Rodrigues, 2004; Rodrigues and Machado,
313 2006). Cell wall components, especially the pattern of cellulose deposition, are indeed responsible for
314 the localization and/or mobility of transmembrane proteins (Martinière et al., 2012; Li et al., 2021).
315 Like pits, pulvinar slits may also affect the localization of ion-channel proteins and/or aquaporins to
316 facilitate water exchange across the cell membrane and modulate cell volume. To clarify the detailed
317 physiological role of pulvinar slits, molecular biological analyses will be needed.
318 Considering all the data described here, pulvinar slits can be characterized as a structurally and
319 mechanically unique property of the cell wall. A unique cell wall structure is linked with the function
320 of several tissues. For example, cellulose and other components of the SCW are deposited in spiral,
321 reticulate, scalariform, or pitted patterns in xylem vessels (Oda and Fukuda, 2012a). The cellulose
322 synthase complex assembles a single cellulose polymer at the plasma membrane and associates with
323 microtubules (Paredez et al., 2006). SCW-type cellulose synthase complexes localize at the
324 presumptive area of the SCW in xylem vessels (Watanabe et al., 2015). The deposition pattern of the
325 SCW is controlled by MICROTUBULE DEPLETION DOMAIN 1 and a Rho-GTPase ROP in
326 metaxylem cells (Oda and Fukuda, 2012b). By analogy, the unique cellulose pattern seen in the CMCs
327 of pulvini might be controlled by the localization of cellulose synthase complexes as well. However,
328 unlike xylem vessels with a thicker SCW, variation in cell wall thickness has not been reported in the

CMCs of pulvini. These differences may be derived from the high accumulation of de-methyl-esterified HG in the slits, which would suggest that the underlying mechanism establishing the unique cell wall pattern of CMCs may be considerably different from that of xylem vessels.

The repeatability and reversibility of legume leaf movements are in sharp contrast to other types of organ movement driven by growth or by mechanical instability. The cellular basis of the repeated and reversible stomatal movements driven by turgor has been extensively studied. Stomata are composed of a pair of guard cells on the leaf epidermis that control gas exchange and repeatedly adjust their aperture by modulating the activity of transmembrane ion channels in response to environmental signals (Kollist et al., 2014). Guard cells have unique morphological features, for example, a kidney-like shape in many eudicots or a dumbbell-like shape in grasses. Major components of primary cell walls, e.g., cellulose, xyloglucan, and pectin, contribute to stomatal movements (Rui and Anderson, 2016; Amsbury et al., 2016; Yi et al., 2018), and computational model-based analyses have demonstrated that cellulose-based anisotropy and polar stiffening of stomata are important factors (Carter et al., 2017; Woolfenden et al., 2017; Woolfenden et al., 2018). The cell wall of guard cells is low in highly methyl-esterified HG and rich in de-esterified HG, a composition similar to that of the inside of pulvinar slits. Notably, de-methyl-esterification of homogalacturonan is required for stomatal function (Amsbury et al., 2016). As with guard cells, we propose that the unique deposition pattern of cell wall components plays an important role in the repeated and reversible deformation of the CMC cell wall that is driven by turgor pressure during leaf movement. Meanwhile, the spatial arrangement of cell wall components significantly different between CMCs and guard cells supports the idea that a unique slit-like pattern has a role in conversion of non-directional inputs (turgor pressure) into directional outputs (biased cell deformations).

Finally, it is worth noting that we observed slits in all pulvini analyzed. This finding raises the possibility that the presence of the slit itself might be one of the physical prerequisites for dynamic leaf movement; slits may therefore cooperate with the regulatory mechanism of turgor pressure that has been elucidated in recent years. Furthermore, from a broader perspective, it is intriguing that CMCs with pulvinar slits are structurally analogous to kirigami (Japanese art of paper cutting), a typical kind of which has many straight cuttings, i.e., slits. Slits of kirigami increase extensibility of the sheet and prevent unpredictable local structural failures (Shyu et al., 2015; Isobe and Okumura, 2016). In conclusion, we propose that pulvinar slits are an example of specialization in motor organs. Our findings provide a new insight into the structural diversity of the cell wall and its association with the mechanical regulation of plant movement.

Methods

Plant materials

Plants used in this study were prepared by four different conditions; outdoor collection of wild plants,

365 outdoor cultivation, indoor cultivation and greenhouse cultivation (Supplemental Table 1). Wild plants
366 of *D. paniculatum*, Persian silk tree (*Albizia julibrissin*), and *white clover (Trifolium repens*) were
367 collected outdoors in Nara, Japan (34°43.5'N, 135°44.1'E), in the summer of 2019 or 2021. Adzuki
368 bean (*Vigna angularis*) Dainagon (TOHOKU SEED Co., Ltd, Japan), cowpea (*Vigna unguiculate*)
369 Sansyaku (TOHOKU SEED Co., Ltd, Japan), common bean (*Phaseolus vulgaris*) L. cv *Morocco*
370 (Atariya Noen Co. Ltd, Japan or TAKII & Co., Ltd, Japan) and sword bean (*Canavalia gladiate*)
371 (Atariya Noen Co. Ltd, Japan or TAKII & Co., Ltd, Japan) were grown outdoors and collected in the
372 summer of 2019. Sensitive plant (*Mimosa pudica*) Wase (SAKATA SEED CORPORATION, Japan),
373 common licorice (*Glycyrrhiza glabra*) (purchased at a garden store) and carob (*Ceratonia siliqua*)
374 (purchased at a garden store) were grown under SMD 5050 white LED light (Samsung) at 100-200
375 μmolm^{-2}s^{-1} under long-day condition (16h light/ 8h dark). Plants of soybean (*Glycine max*) and *Lotus*
376 *japonicus* were grown in the greenhouse of NAIST adjusted to long-day condition by supplementary
377 light. Except for species collected outdoors, potted plants of all tested species were grown on culture
378 soil (Kohnan Shoji Co.,Ltd. or Nihon Hiryo Co.,Ltd). Samples were harvested at Zeitgeber time (ZT)
379 2–7.
380
381 **Staining and microscopy**
382 Leaves with pulvini were fixed in FAA solution (5% [v/v] formaldehyde, 5% [v/v] acetic acid, 45%
383 [v/v] ethanol) or PFA solution (2.22% [w/v] paraformaldehyde, 0.5 M mannitol, 50 mM PIPES, pH
384 6.9) and stored at 4°C. For the analysis of *D. paniculatum* (Figure 1) and nine other species (excluding
385 *L. japonicus*), fixed samples were transferred into distilled water several hours before analysis and
386 sliced with a single-edged razor. For analyses of *D. paniculatum* (Figures 2, 3, Supplemental Figure
387 2) and *L. japonicus*, fixed samples were washed in distilled water several times, embedded in 5% (w/v)
388 agarose gel, and sliced into 100-μm sections with a MicroSlicer Zero 1 (DOSAKA EM, Kyoto, Japan).
389 For calcofluor white staining, the sections were placed on glass slides, treated with one drop of
390 calcofluor white stain solution (Sigma-Aldrich, USA) and one drop of 10% (w/v) potassium hydroxide
391 for 1 min, mounted in distilled water, and covered by a cover slip, before observations with a confocal
392 laser scanning microscope (LSM800, Zeiss, Germany) equipped with a Plan-Apochromat 20x/0.8
393 M27 objective lens (Zeiss, Germany; excitation 405 nm; emission 400–560 nm). For whole-mount
394 observations of *L. japonicus* pulvini, fixed samples were transferred into 1x phosphate buffered saline
395 (PBS), pH 7.5 (130 mM NaCl, 7 mM Na_2HPO_4, and 3 mM NaH_2PO_4), washed in 1x PBS twice, soaked
396 in ClearSee solution (10% [w/v] xylitol, 15% [w/v] sodium deoxycholate, and 25% [w/v] urea)
397 (Kurihara et al., 2015) for 1 week, stained with 2.5 μg/mL calcofluor white in ClearSee solution for 5
398 d, mounted in ClearSee solution, and observed under a LSM800 as described above.
399 For pontamine staining, the sections were incubated with 50 mg/L Direct Fast Scarlet 4BS (Wako,
400 Japan) for 20 min, rinsed with 100 mM $NaPO_4$ buffer several times, mounted in distilled water, and

401 covered by a cover slip, before observations with a LSM800 equipped with a Plan-Apochromat
402 20x/0.8 M27 objective lens (excitation 488 nm; emission 560–605 nm).
403 For immunostaining, sections were rinsed with Tris-buffered saline (TBS, 20 mM Tris-HCl, 150 mM
404 NaCl, pH 7.5) three times, incubated in blocking solution (1% [w/v] bovine serum albumin, 1% [w/v]
405 normal goat serum (abcam ab7481) in TBS with 0.2% [v/v] Tween-20 [TBST]), rinsed with TBST
406 three times, treated with TBS (for no antibody control) and with primary antibodies (JIM7, LM19,
407 2F4, PlantProbes, diluted 1:10) in TBS at 4°C for 1 h, rinsed with TBST three times, incubated with
408 secondary antibodies (anti-rat IgG-CFL488, anti-mouse IgG-Alexa488, anti-His tag IgG-CFL488, all
409 diluted 1:100) at 4°C for 1 h, and rinsed with TBST five times. The samples were mounted with 1 mL
410 TBST with 10 μL calcofluor white stain solution and 10 μL of 10% (w/v) potassium hydroxide,
411 covered by a cover slip, and observed with a LSM800 equipped with a Plan-Apochromat 20x/0.8 M27
412 or Plan-Apochromat 100x/1.46 Oil objective lens (excitation 488 nm; emission 400–575 nm;
413 excitation 405 nm; emission 400–510 nm).
414
415 **Cell wall analysis**
416 Primary pulvini, secondary pulvini, petioles, young stems, and mature stems of *D. paniculatum* were
417 harvested for analysis of cell wall composition. Preparation of cell wall residues and monosaccharide
418 composition analysis were performed as previously described (Sakamoto et al., 2015). Fourier-
419 transform infrared spectroscopy (FTIR) analysis was performed as described previously (Sakamoto et
420 al., 2018).
421
422 **Computational modeling**
423 The finite-element method (FEM) was implemented based on previously reported FEM models
424 (Bonazzi et al., 2014; Hong et al., 2016; Tsugawa, 2020). Using FEM, cell deformation under uniform
425 pressure was confirmed, which indicates a mechanically unstable orientation depending on the internal
426 structure. To adjust the models with our observations, the initial internal structure was set as one of
427 the following three types: 1) cells with four slits with different slit anisotropy; 2) cells with different
428 numbers of slits but with the same slit anisotropy; or 3) cells with four slits with different slit areas.
429 The cell contour was set to be a regular hexagon, and the side of the hexagon was set to 10 arbitrary
430 units (au), which was assumed to be micrometers in live cells. With these initial conditions and certain
431 mechanical properties (Young's modulus 1 MPa and Poisson's ratio 0.35), the cells were uniformly
432 pressurized with turgor pressure. Increases in the parameters $E = 1, 5, 10$ (MPa) and $\nu =$
433 $0.35, 0.4, 0.45$ resulted in small deformations, but the overall trend of all three cases was qualitatively
434 similar. We also assumed that the small deformation and the constitutive law follow the generalized
435 Hooke's law. When cells were pressurized with a turgor pressure $P = 0.1$ (MPa) to match the typical
436 scale of previously reported turgor pressure, the cells slightly expanded depending on the slit structure.

437 As with changes in the mechanical parameters, changes in turgor pressure ($P = 0.2, 0.3$) did not
438 qualitatively differ from those with $P = 0.1$.
439
440 **Compression test of pulvini and other axial organs**
441 Each organ was excised into segments of approximately 2 mm in length just before the test. Load
442 while giving a constant-speed deformation (0.05 mm/s) was measured with a RHEONERII creep
443 meter (Yamaden, Japan; RE2-3305C) equipped with a 20 N load cell. Excised specimens were placed
444 on a moving platform with the apex-base axis as the horizontal axis and compressed by sandwiching
445 each specimen between the moving platform and a cylindrical plunger with a diameter of 3 mm. Strain
446 was calculated by dividing the deformation by the height at time 0. Analyses were conducted in the
447 daytime on the same day as sample collection.
448 To measure the PD extension, videos were captured during the compression test with a 10–200x
449 magnification USB digital microscope (Giwox, China) and the PhotoBooth App (Apple, USA).
450 Captured videos were divided into frames with ffmpeg software (https://ffmpeg.org/). Images at the
451 time of each 10% strain were selected based on their frame rate and the height at time 0. The PD length
452 of each organ was manually measured with ImageJ (Fiji; https://fiji.sc/) and the extension ratio was
453 calculated by the following equation in Microsoft Excel.

454 $$Extension\ ratio = \frac{L_n - L_0}{L_0}$$

455 where L_0 represents the length when strain is 0 and L_n represents the length when strain is n (0.1-
456 0.8).
457 For the observation of the spreading of tiny wrinkles in the epidermis upon compression, videos were
458 captured with a HiVision Microscope FZ200BA equipped with HDMI recorder X Capture MINI
459 (Shodensha, Japan).
460 For observations of loaded pulvini, prior to observation, tissues were manually compressed with a
461 10 N load while measuring with an electronic balance. For observations by scanning electron
462 microscopy, tissues were frozen in liquid nitrogen for 15 s and were observed with a FEI Quanta 250
463 scanning electron microscope (ThermoFisher Scientific, USA). For observations by confocal laser
464 microscopy, fresh samples embedded in 6% (w/v) agarose gel were sliced into 50-μm sections with a
465 MicroSlicer Zero 1. For calcofluor white staining, the 50-μm sections were observed by the same
466 procedure as when observing CMCs. For visualization of lignin autofluorescence, unstained sections
467 were mounted in distilled water and a cover glass. Sections were observed with a LSM800 as described
468 above.
469
470 **Statistical analyses**
471 Microsoft Excel for Mac v16.16.11 (Microsoft, USA) or the Python language v3.7.2

472 (https://www.python.org/) and Python packages/libraries including Pandas v0.23.4
473 (https://pandas.pydata.org/), NumPy v1.16.4 (https://www.numpy.org/), Matplotlib v2.2.3
474 (https://matplotlib.org/), Seaborn v0.9.0 (https://seaborn.pydata.org/), and Statsmodels v0.9.0
475 (https://www.statsmodels.org/stable/) were used for statistical analyses.
476
477 **References**

478 **Amsbury S, Hunt L, Elhaddad N, Baillie A, Lundgren M, Verhertbruggen Y, Scheller HV, Knox JP,**
479 **Fleming AJ, Gray JE** (2016) Stomatal Function Requires Pectin De-methyl-esterification of the
480 Guard Cell Wall. Curr Biol **26:** 2899-2906
481 **Azani N, Babineau M, Bailey D, C., Banks H, Barbosa R, Ariane, Pinto B, Rafael, Boatwright S,**
482 **James, Borges M, Leonardo, Brown K, Gillian, Bruneau A, Candido E, Cardoso D, Chung K-**
483 **F, Clark P, Ruth, Conceição S, de, Adilva, Crisp M, Cubas P, Delgado-Salinas A, Dexter G,**
484 **Kyle, Doyle J, Jeff, Duminil J, Egan N, Ashley, Estrella l, de, Manuel, Falcão J, Marcus,**
485 **Filatov A, Dmitry, Fortuna-Perez P, Ana, Fortunato H, Renée, Gagnon E, Gasson P, Rando G,**
486 **Juliana, Tozzi A, de, Goulart, Maria, Ana, Gunn B, Harris D, Haston E, Hawkins A, Julie,**
487 **Herendeen S, Patrick, Hughes E, Colin, Iganci RV, João, Javadi F, Kanu A, Sheku,**
488 **Kazempour-Osaloo S, Kite C, Geoffrey, Klitgaard B, Bente, Kochanovski J, Fábio, Koenen**
489 **JM, Erik, Kovar L, Lavin M, Roux l, Marianne, Lewis P, Gwilym, Lima d, C., Haroldo,**
490 **López-Roberts C, Maria, Mackinder B, Maia H, Vitor, Malécot V, Mansano F, Vidal, Marazzi**
491 **B, Mattapha S, Miller T, Joseph, Mitsuyuki C, Moura T, Murphy J, Daniel, Nageswara-Rao**
492 **M, Nevado B, Neves D, Ojeda I, Dario, Pennington T, R., Prado E, Darién, Prenner G,**
493 **Queiroz d, Paganucci, Luciano, Ramos G, Filardi R, L., Fabiana, Ribeiro G, Pétala, Rico-Arce**
494 **L, de, María, Sanderson J, Michael, Santos-Silva J, São-Mateus MB, Wallace, Silva JS,**
495 **Marcos, Simon F, Marcelo, Sinou C, Snak C, Souza d, R., Élvia, Sprent J, Steele P, Kelly,**
496 **Steier E, Julia, Steeves R, Stirton H, Charles, Tagane S, Torke M, Benjamin, Toyama H, Cruz**
497 **d, Trabuco, Daiane, Vatanparast M, Wieringa J, Jan, Wink M, Wojciechowski F, Martin,**
498 **Yahara T, Yi T, Zimmerman E** (2017) A new subfamily classification of the Leguminosae based
499 on a taxonomically comprehensive phylogeny: The Legume Phylogeny Working Group (LPWG).
500 Taxon **66:** 44-77 , DOI = 10.12705/12661.12703
501 **Bonazzi D, Julien JD, Romao M, Seddiki R, Piel M, Boudaoud A, Minc N** (2014) Symmetry breaking in
502 spore germination relies on an interplay between polar cap stability and spore wall mechanics. Dev
503 Cell **28:** 534-546
504 **Carter R, Woolfenden H, Baillie A, Amsbury S, Carroll S, Healicon E, Sovatzoglou S, Braybrook S,**
505 **Gray JE, Hobbs J, Morris RJ, Fleming AJ** (2017) Stomatal Opening Involves Polar, Not Radial,
506 Stiffening Of Guard Cells. Curr Biol **27:** 2974-2983.e2972
507 **Cosgrove DJ** (2005) Growth of the plant cell wall. Nat Rev Mol Cell Biol **6:** 850-861

508 **Cosgrove DJ** (2018) Diffuse Growth of Plant Cell Walls. Plant Physiol **176:** 16-27
509 **Darwin C, Darwin F** (1880) The power of movement in plants, Chapter VII. John Murray, London
510 **Du J, Lu S, Chai M, Zhou C, Sun L, Tang Y, Nakashima J, Kolape J, Wen Z, Behzadirad M, Zhong T,**
511 **Sun J, Zhang Y, Wang ZY** (2021) Functional characterization of *PETIOLULE-LIKE PULVINUS*
512 (*PLP*) gene in abscission zone development in *Medicago truncatula* and its application to genetic
513 improvement of alfalfa. Plant Biotechnol J **19:** 351-364
514 **Dumais J, Forterre Y** (2012) "Vegetable dynamicks" : the role of water in plant movements. Annu Rev
515 Fluid Mech **44:** 453-478 , DOI = 410.1146/annurev-fluid-120710-101200
516 **Fleurat-Lessard P, Bonnemain JL** (1978) Structural and ultrastructural characteristics of the vascular
517 apparatus of the sensitive plant (*Mimosa pudica* L.). Protoplasma **94:** 127-143
518 **Fleurat-Lessard P, Roblin G** (1982) Comparative histocytology of the petiole and the main pulvinus in
519 Mimosa pudica L. Annals of Botany **50:** 83-92
520 **Fleurat-Lessard P, Roblin G** (1988) Structural and ultrastructural features of cortical cells in motor organs
521 of sensitive plants. Biol Rev **63:** 1-22
522 **Gao J, Yang S, Cheng W, Fu Y, Leng J, Yuan X, Jiang N, Ma J, Feng X** (2017) GmILPA1, Encoding an
523 APC8-like Protein, Controls Leaf Petiole Angle in Soybean. Plant Physiol **174:** 1167-1176
524 **Geitmann A** (2016) Actuators Acting without Actin. Cell **166:** 15-17
525 **Geitmann A, Ortega JK** (2009) Mechanics and modeling of plant cell growth. Trends Plant Sci **14:** 467-478
526 **Hong L, Dumond M, Tsugawa S, Sapala A, Routier-Kierzkowska AL, Zhou Y, Chen C, Kiss A, Zhu**
527 **M, Hamant O, Smith RS, Komatsuzaki T, Li CB, Boudaoud A, Roeder AH** (2016) Variable
528 Cell Growth Yields Reproducible Organ Development through Spatiotemporal Averaging. Dev Cell
529 **38:** 15-32
530 **Isobe M, Okumura K** (2016) Initial rigid response and softening transition of highly stretchable kirigami
531 sheet materials. Sci Rep **6:** 24758
532 **Koller D** (1990) Light-driven leaf movements. Plant Cell Environ **13:** 615-632 , DOI = 610.1111/j.1365-
533 3040.1990.tb01079.x
534 **Kollist H, Nuhkat M, Roelfsema MR** (2014) Closing gaps: linking elements that control stomatal
535 movement. New Phytol **203:** 44-62
536 **Kurihara D, Mizuta Y, Sato Y, Higashiyama T** (2015) ClearSee: a rapid optical clearing reagent for
537 whole-plant fluorescence imaging. Development **142:** 4168-4179
538 **Li H, von Wangenheim D, Zhang X, Tan S, Darwish-Miranda N, Naramoto S, Wabnik K, De Rycke R,**
539 **Kaufmann WA, Gütl D, Tejos R, Grones P, Ke M, Chen X, Dettmer J, Friml J** (2021) Cellular
540 requirements for PIN polar cargo clustering in *Arabidopsis thaliana*. New Phytol **229:** 351-369
541 **Machado SR, Rodrigues TM** (2004) Anatomia e ultra-estrutura do pulvino primário de Pterodon pubescens
542 Benth. (Fabaceae – Faboideae). Rev Bras Bot **27:** 135-147
543 **Martinière A, Lavagi I, Nageswaran G, Rolfe DJ, Maneta-Peyret L, Luu DT, Botchway SW, Webb SE,**

Mongrand S, Maurel C, Martin-Fernandez ML, Kleine-Vehn J, Friml J, Moreau P, Runions J (2012) Cell wall constrains lateral diffusion of plant plasma-membrane proteins. Proc Natl Acad Sci U S A **109:** 12805-12810

Mayer WE, Flach D, Raju MV, Starrach N, Wiech E (1985) Mechanics of circadian pulvini movements in *Phaseolus coccineus* L. : Shape and arrangement of motor cells, micellation of motor cell walls, and bulk moduli of extensibility ([Formula: see text]). Planta **163:** 381-390

Mitra PP, Loqué D (2014) Histochemical staining of *Arabidopsis thaliana* secondary cell wall elements. J Vis Exp

Moran N (2007) Osmoregulation of leaf motor cells. FEBS Lett **581:** 2337-2347

Moysset L, Llambrich E, Simón E (2019) Calcium changes in *Robinia pseudoacacia* pulvinar motor cells during nyctinastic closure mediated by phytochromes. Protoplasma **256:** 615-629

Moysset L, Simon E (1991) Secondary pulvinus of *Robinia pseudoacacia* (leguminosae): structural an ultrastructural features. Am J Bot **78:** 1467-1486, DOI = 1410.2307/2444972

O'Brien TP, Feder N, McCully ME (1964) Polychromatic Staining of Plant Cell Walls by Toluidine Blue. Protoplasma **59:** 368-373

Oda Y, Fukuda H (2012a) Secondary cell wall patterning during xylem differentiation. Curr Opin Plant Biol **15:** 38-44

Oda Y, Fukuda H (2012b) Initiation of cell wall pattern by a Rho- and microtubule-driven symmetry breaking. Science **337:** 1333-1336

Paredez AR, Somerville CR, Ehrhardt DW (2006) Visualization of cellulose synthase demonstrates functional association with microtubules. Science **312:** 1491-1495

Rodrigues TM, Machado SR (2006) Anatomia comparada do pulvino prim · rio de leguminosas com diferentes velocidades de movimento foliar. Rev Bras Bot **29:** 709-720

Rui Y, Anderson CT (2016) Functional Analysis of Cellulose and Xyloglucan in the Walls of Stomatal Guard Cells of Arabidopsis. Plant Physiol **170:** 1398-1419

Sakamoto S, Somssich M, Nakata MT, Unda F, Atsuzawa K, Kaneko Y, Wang T, Bågman AM, Gaudinier A, Yoshida K, Brady SM, Mansfield SD, Persson S, Mitsuda N (2018) Complete substitution of a secondary cell wall with a primary cell wall in Arabidopsis. Nat Plants **4:** 777-783

Sakamoto S, Yoshida K, Sugihara S, Mitsuda N (2015) Development of a new high-throughput method to determine the composition of ten monosaccharides including 4-O-methyl glucuronic acid from plant cell walls using ultra-performance liquid chromatography. Plant Biotechnol **32:** 55-63

Shyu TC, Damasceno PF, Dodd PM, Lamoureux A, Xu L, Shlian M, Shtein M, Glotzer SC, Kotov NA (2015) A kirigami approach to engineering elasticity in nanocomposites through patterned defects. Nat Mater **14:** 785-789

Smithers ET, Luo J, Dyson RJ (2019) Mathematical principles and models of plant growth mechanics: from cell wall dynamics to tissue morphogenesis. J Exp Bot **70:** 3587-3600

580 **Song K, Yoem E, Lee SJ** (2014) Real-time imaging of pulvinus bending in *Mimosa pudica*. Sci. Rep. **4:**
581 6466
582 **Tsugawa S** (2020) Suppression of soft spots and excited modes in the shape deformation model with spatio-
583 temporal growth noise. J Theor Biol **486:** 110092
584 **Wang X, Wilson L, Cosgrove DJ** (2020) Pectin methylesterase selectively softens the onion epidermal wall
585 yet reduces acid-induced creep. J Exp Bot **71:** 2629-2640
586 **Watanabe Y, Meents MJ, McDonnell LM, Barkwill S, Sampathkumar A, Cartwright HN, Demura T,**
587 **Ehrhardt DW, Samuels AL, Mansfield SD** (2015) Visualization of cellulose synthases in
588 Arabidopsis secondary cell walls. Science **350:** 198-203
589 **Weintraub M** (1952) Leaf movements in *Mimosa pudica* L. New Phytol **50:** 357-382
590 **Woolfenden HC, Baillie AL, Gray JE, Hobbs JK, Morris RJ, Fleming AJ** (2018) Models and
591 Mechanisms of Stomatal Mechanics. Trends Plant Sci **23:** 822-832
592 **Woolfenden HC, Bourdais G, Kopischke M, Miedes E, Molina A, Robatzek S, Morris RJ** (2017) A
593 computational approach for inferring the cell wall properties that govern guard cell dynamics. Plant J
594 **92:** 5-18
595 **Yi H, Rui Y, Kandemir B, Wang JZ, Anderson CT, Puri VM** (2018) Mechanical Effects of Cellulose,
596 Xyloglucan, and Pectins on Stomatal Guard Cells of. Front Plant Sci **9:** 1566
597 **Zhang Y, Tang H, Vavylonis T, Cosgrove DJ** (2019) Disentangling loosening from softening: insights into
598 primary cell wall structure. Plant J **100:** 1101-1117
599 **Zheng Y, Wang X, Chen Y, Wagner E, Cosgrove DJ** (2018) Xyloglucan in the primary cell wall:
600 assessment by FESEM, selective enzyme digestions and nanogold affinity tags. Plant J **93:** 211-226
601 **Zhou C, Han L, Fu C, Chai M, Zhang W, Li G, Tang Y, Wang ZY** (2012) Identification and
602 characterization of petiolule-like pulvinus mutants with abolished nyctinastic leaf movement in the
603 model legume *Medicago truncatula*. New Phytol. **196(1):** 92-100
604

605 **Acknowledgements and funding**

606 We thank Kiyotaka Okada (Ryukoku Univ., Japan) and Nobutaka Mitsuda (AIST, Japan) for helpful
607 comments, Atsunobu Suzuki (NAIST, Japan), Hitomi Ichikawa (NAIST, Japan) and Aeni Hosaka
608 (AIST, Japan) for technical support. We thank Tadashi Kunieda (NAIST, Japan), Ko Kato (NAIST,
609 Japan) and members of the Demura lab for general support during experiments. *G. max* seeds were
610 obtained from LegumeBase (http://www.legumebase.brc.miyazaki-u.ac.jp/), which is supported by
611 the National BioResource Project (NBRP) in Japan. We thank Plant Editors (https://planteditors.com/)
612 for English-language editing.
613 This work was supported by JSPS KAKENHI Grant Numbers JP20K15832 (to S.T.), JP19K16174
614 (to S.S.), JP19K23753 (to M.N.) and JP20K06707 (to M.N.), and by MEXT KAKENHI Grant-in-Aid
615 for Scientific Research on Innovative Areas “Plant-Structure Optimization Strategy” Grant Numbers

JP18H05484 and JP18H05489 (to T.D.).

Author Contributions

M.T and M.T.N. contributed conception and design of the study, performed biological/histochemical/mechanical experiments and image/statistical analyses, and wrote the first draft of the manuscript. S.T. performed FEM analysis and wrote the section of FEM simulation. S.S. performed FTIR and monosaccharide analysis, contributed the data interpretation, and wrote the section of cell-wall assay. T.D. contributed significantly the revision of the experimental design and the modification of the draft. All authors discussed the results and contributed to the final manuscript.

Ethics declarations

Competing interests

The authors declare no competing interest.

Supplemental information

Supplemental figures and table

Figure legends

Figure 1. Calcofluor-white staining of pulvinar cortical motor cells (CMCs) in various legume species. (A) Schematic diagram (left) and photography (right) of a *Desmodium paniculatum* leaf. Pu, primary pulvinus; SPu, secondary pulvinus; Pe, petiole; Ds, developing stem; Ms, mature stem. (B) Schematic diagrams of the collected pulvini and petiole samples for microscopy. Letters C to F indicate the positions visualized in the corresponding panels. (C-F) Sections of calcofluor white-stained *D. paniculatum* pulvini and petioles by confocal laser scanning microscopy. AdAb, adaxial-abaxial axis; PD, proximo-distal axis; ML, medial-lateral axis; ep in F indicates epidermis. (G) A model of pulvinar slits and small spots in the cell wall of a CMC. TPu, a tertiary pulvinus. (H) Vertical sections of calcofluor white-stained pulvinar CMCs from 11 legume species. The vertical direction of all images corresponds to the adaxial-abaxial axis. (I) Whole-mount projection of calcofluor white-stained *L. japonicus* CMCs (top). Middle, magnified view of the orange square. Bottom, optical Z-section shown as the blue line in the middle panel. Arrowheads indicate pulvinar slits. Bars, 2 cm (A), or 20 μm (C-F, H, I).

Figure 2. Visualization of cellulose in *D. paniculatum* pulvinar CMCs.

(A) Pontamine-stained CMCs of a *D. paniculatum* pulvinus (vertical section). (B) Co-localization of calcofluor white signal (CF) and staining with the CBM3a antibody (recognizing crystalline cellulose) in CMCs in a vertical section of a *D. paniculatum* pulvinus. Arrowheads, pulvinar slits. Bars, 20 μm.

652

653 **Figure 3**. Immuno-histological analyses of *D. paniculatum* pulvinar CMCs.

654 (A) Immuno-labeled CMCs with antibodies against primary cell wall (PCW) components in vertical
655 sections. These samples were co-stained with calcofluor white (CF). Asterisk indicates a tannin
656 vacuole. (B-C) Magnified views of dashed boxes in (A) (left) and profiles of relative intensities for
657 calcofluor white (blue) and antibody signal (green) along the yellow lines in the magnified images
658 (right). Bars, 20 μm (A).

659

660 **Figure 4**. Cell wall assay of *D. paniculatum* axial organs.

661 (A) FTIR spectra of cell wall components obtained from five different axial organs: primary pulvini
662 (Pu), secondary pulvini (SPu), petioles (Pe), developing stems (Ds), and mature stems (Ms), as six
663 biological replicates. Data are shown as the mean and 95% confidence interval. (B) Principal
664 component analysis applied to the FTIR spectra shown in A. (C) The heatmap with dendrogram for
665 the relative amount of each monosaccharide in each organ. Color indicates the ratio to the mean in
666 each monosaccharide. Gal, galactose; GalA, galacturonic acid; Ara, arabinose; Fuc, fructose; GlcA,
667 glucuronic acid; Man, mannose; Rha, rhamnose; Glc, glucose; Xyl, xylose.

668

669 **Figure 5**. Computational modeling of the expansion of a hexagonal cell with slits.

670 (A) Schematic diagram of the hexagonal cells with definition of terms used. (B) Relative length and
671 width of 59 slits from eight species: *D. paniculatum*, *P. vulgaris*, *V. angularis*, *V. unguiculata*, *G. max*
672 (Jack), *A. julibrissin*, *M. pudica*, and *C. siliqua*. (C) Color key for principal direction of growth shown
673 in D, F, and H. 0, horizontal plane; $\pi/2$, vertical plane. (D-I) Results of FEM simulations to clarify the
674 effect of slit direction (D, E), slit number (F, G), or slit size (H, I). In D, F, and H, the upper panels
675 indicate finite element mesh, and the lower panels indicate the final shape and the principal direction
676 of growth. er_x, extension ratio along the x (horizontal) axis; er_y, extension ratio along the y (vertical)
677 axis; r_x, slit length along the x-axis; r_y, slit length along the y-axis.

678

679 **Figure 6**. Compression test of pulvini and other axial organs.

680 (A) Ratio of the PD extension of the axial organs for each strain applied. N = 18 (pulvini, Pu), 10
681 (petioles, Pe), 15 (developing stems, Ds), 10 (mature stems, Ms, other than strain = 0.7), and 8 (mature
682 stems, strain = 0.7). Different letters indicate statistical differences (Tukey's HSD test, family-wise
683 error rate = 0.05). (B) Ratio of the PD extension of the axial organs in *D. paniculatum* when the applied
684 strain is 0.5. (C) Ratio of the PD extension of axial organs in three other species when the applied
685 strain is 0.5. N = 15 (*P. vulgaris* petioles), 16 (*P. vulgaris* pulvini), 12 (*V. angularis*), and 11 (*V.*
686 *unguiculata*). $^{***}p < 0.001$ by two-sided Welch's *t*-test. The calculated t-statistics for *P. vulgaris*, *V.*
687 *angularis*, and *V. unguiculata* are 12.20, 9.04, and 9.05, respectively. (D) Serial images of side views

688 of *D. paniculatum* pulvini during compression with a creep meter.

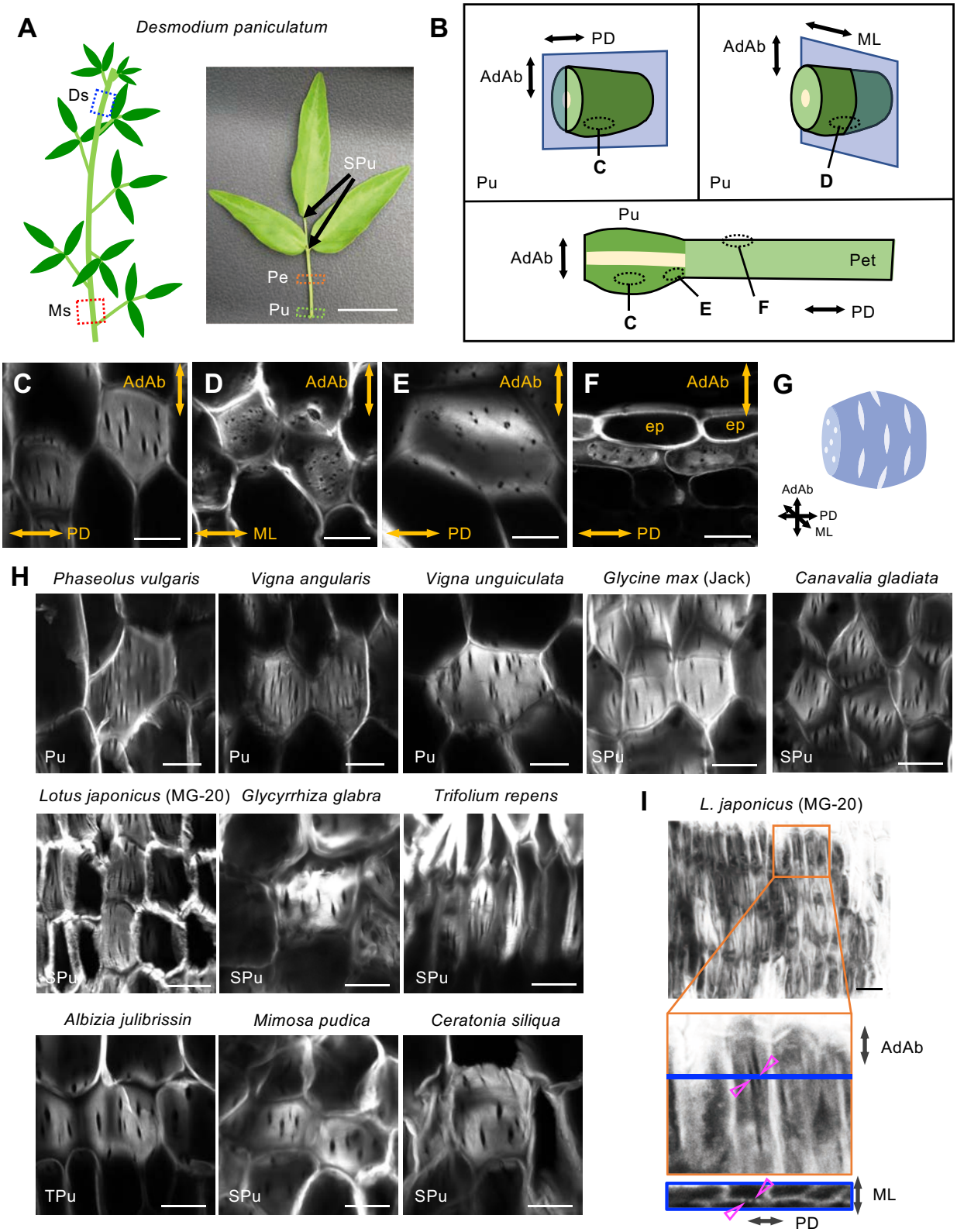

Figure 1. Calcofluor-white staining of pulvinar cortical motor cells (CMCs) in various legume species.

(A) Schematic diagram (left) and photography (right) of a *Desmodium paniculatum* leaf. Pu, primary pulvinus; SPu, secondary pulvinus; Pe, petiole; Ds, developing stem; Ms, mature stem. (B) Schematic diagrams of the collected pulvini and petiole samples for microscopy. Letters C to F indicate the positions visualized in the corresponding panels. (C-F) Sections of calcofluor white-stained *D. paniculatum* pulvini and petioles by confocal laser scanning microscopy. AdAb, adaxial-abaxial axis; PD, proximo-distal axis; ML, medial-lateral axis; ep in F indicates epidermis. (G) A model of pulvinar slits and small spots in the cell wall of a CMC. TPu, a tertiary pulvinus. (H) Vertical sections of calcofluor white-stained pulvinar CMCs from 11 legume species. The vertical direction of all images corresponds to the adaxial-abaxial axis. (I) Whole-mount projection of calcofluor white-stained *L. japonicus* CMCs (top). Middle, magnified view of the orange square. Bottom, optical Z-section shown as the blue line in the middle panel. Arrowheads indicate pulvinar slits. Bars, 2 cm (A), or 20 μm (C-F, H, I).

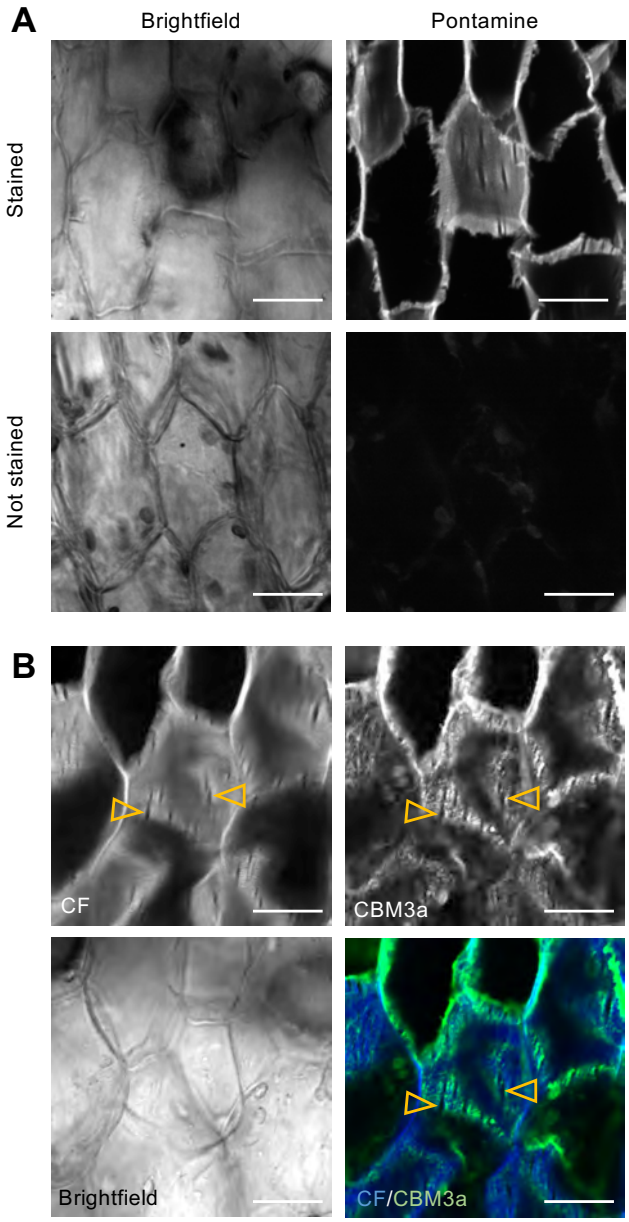

Figure 2. Visualization of cellulose in *D. paniculatum* pulvinar CMCs.

(A) Pontamine-stained CMCs of a *D. paniculatum* pulvinus (vertical section). (B) Co-localization of calcofluor white signal (CF) and staining with the CBM3a antibody (recognizing crystalline cellulose) in CMCs in a vertical section of a *D. paniculatum* pulvinus. Arrowheads, pulvinar slits. Bars, 20 μm.

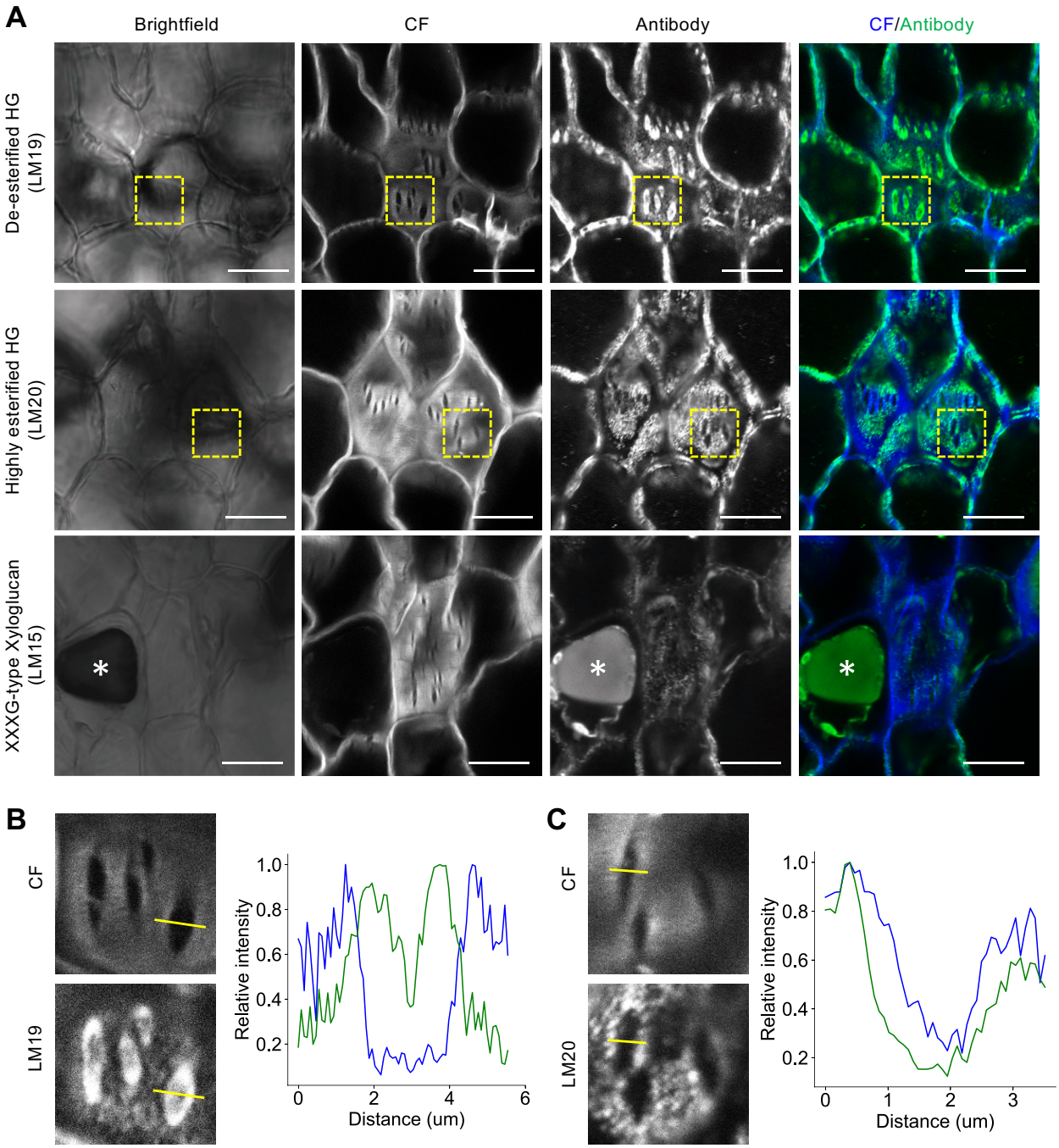

Figure 3. Immuno-histological analyses of *D. paniculatum* pulvinar CMCs.

(A) Immuno-labeled CMCs with antibodies against primary cell wall (PCW) components in vertical sections. These samples were co-stained with calcofluor white (CF). Asterisk indicates a tannin vacuole. (B-C) Magnified views of dashed boxes in (A) (left) and profiles of relative intensities for calcofluor white (blue) and antibody signal (green) along the yellow lines in the magnified images (right). Bars, 20 μm (A).

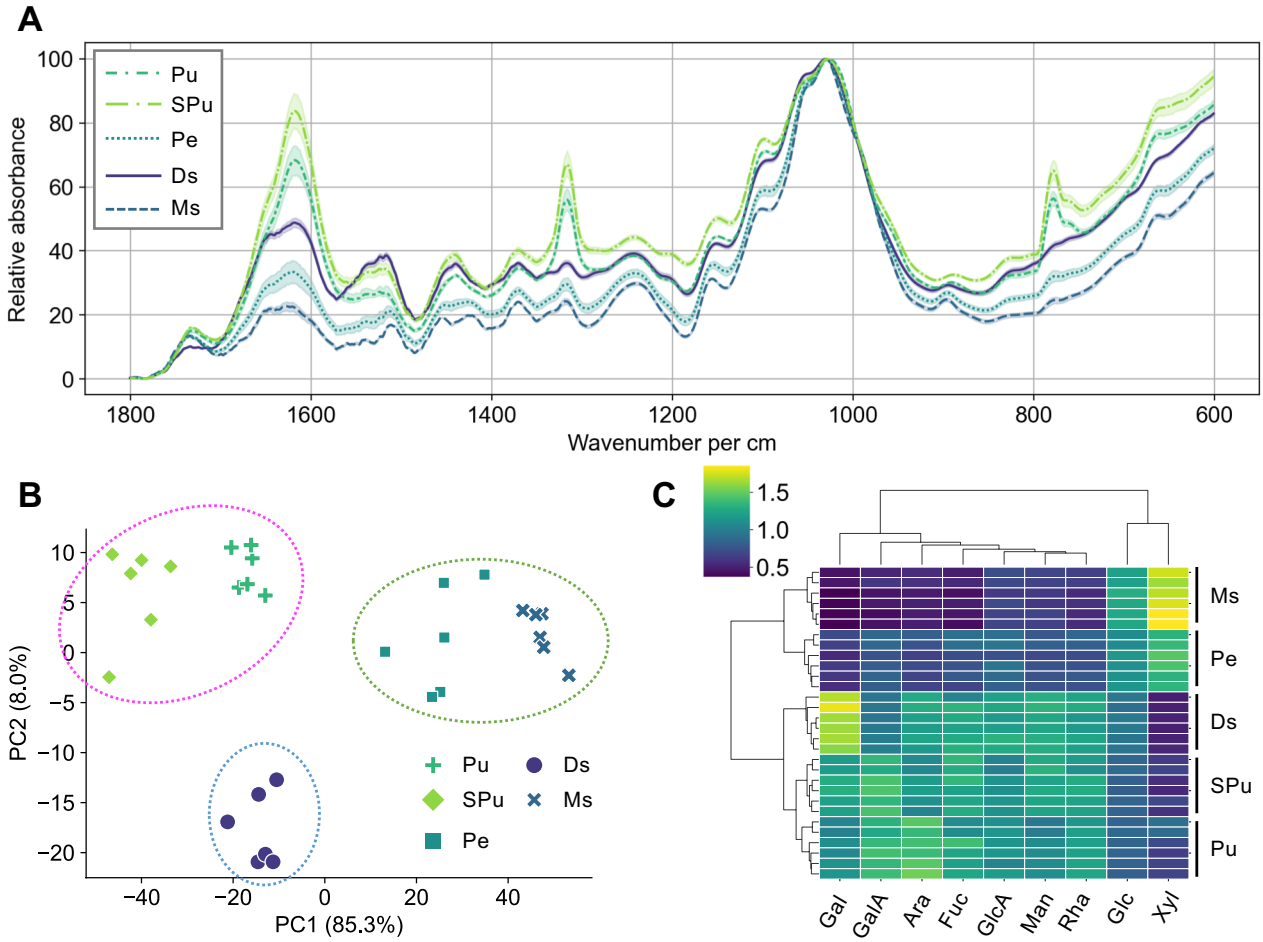

Figure 4. Cell wall assay of *D. paniculatum* axial organs.

(A) FTIR spectra of cell wall components obtained from five different axial organs: primary pulvini (Pu), secondary pulvini (SPu), petioles (Pe), developing stems (Ds), and mature stems (Ms), as six biological replicates. Data are shown as the mean and 95% confidence interval. (B) Principal component analysis applied to the FTIR spectra shown in A. (C) The heatmap with dendrogram for the relative amount of each monosaccharide in each organ. Color indicates the ratio to the mean in each monosaccharide. Gal, galactose; GalA, galacturonic acid; Ara, arabinose; Fuc, fructose; GlcA, glucuronic acid; Man, mannose; Rha, rhamnose; Glc, glucose; Xyl, xylose.

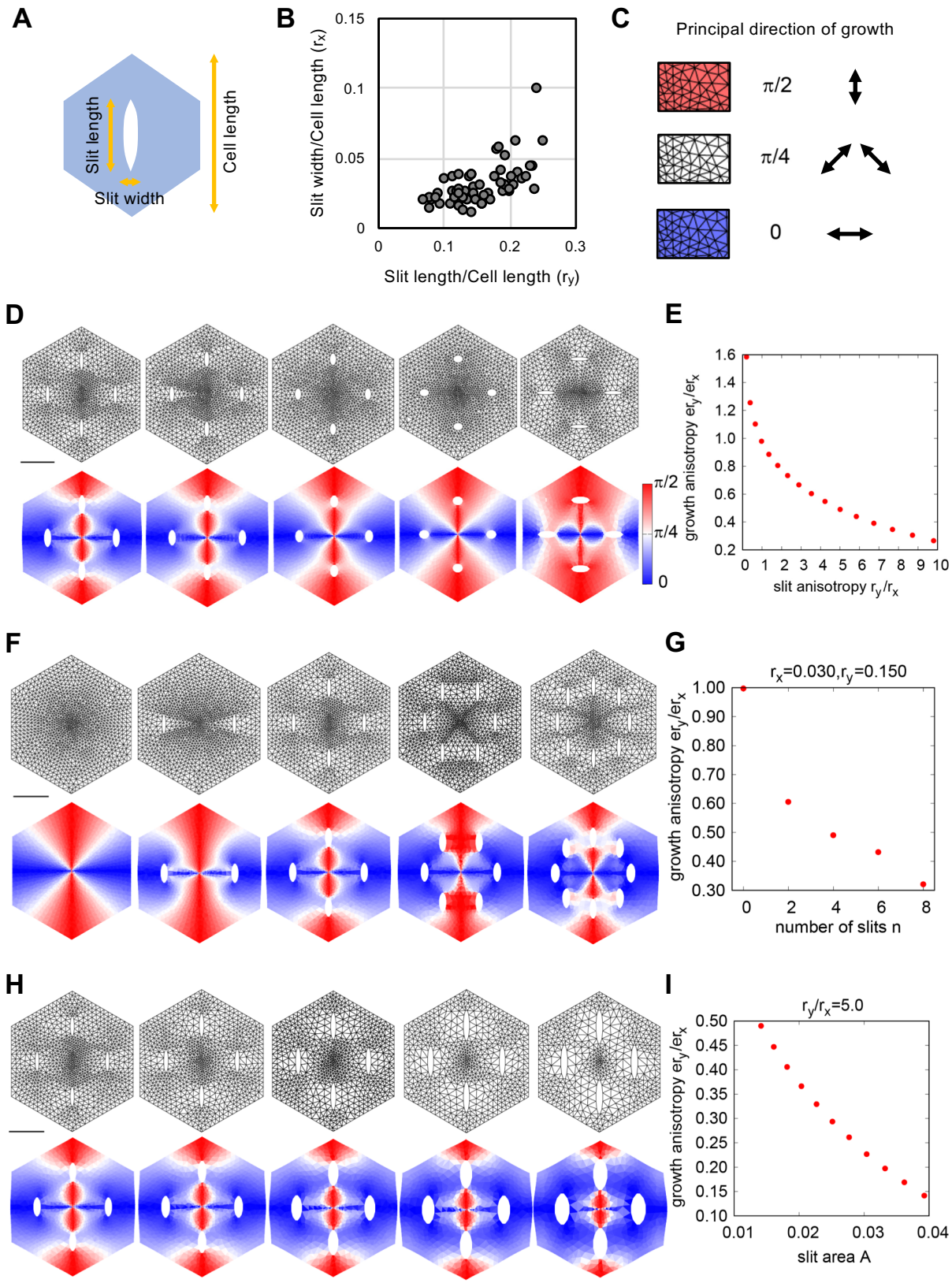

Figure 5. Computational modeling of the expansion of a hexagonal cell with slits.

(A) Schematic diagram of the hexagonal cells with definition of terms used. (B) Relative length and width of 59 slits from eight species: *D. paniculatum*, *P. vulgaris*, *V. angularis*, *V. unguiculata*, *G. max* (Jack), *A. julibrissin*, *M. pudica*, and *C. siliqua*. (C) Color key for principal direction of growth shown in D, F, and H. 0, horizontal plane; π/2, vertical plane. (D-I) Results of FEM simulations to clarify the effect of slit direction (D, E), slit number (F, G), or slit size (H, I). In D, F, and H, the upper panels indicate finite element mesh, and the lower panels indicate the final shape and the principal direction of growth. er_x, extension ratio along the x (horizontal) axis; er_y, extension ratio along the y (vertical) axis; r_x, slit length along the x-axis; r_y, slit length along the y-axis.

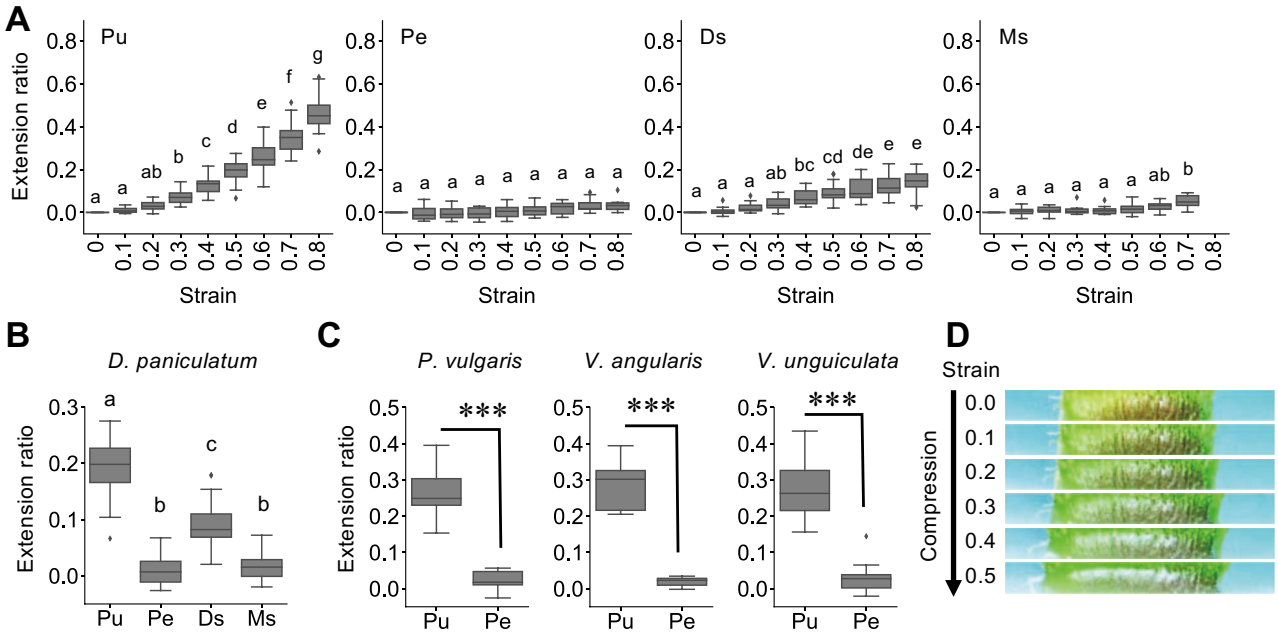

Figure 6. Compression test of pulvini and other axial organs.

(A) Ratio of the PD extension of the axial organs for each strain applied. N = 18 (pulvini, Pu), 10 (petioles, Pe), 15 (developing stems, Ds), 10 (mature stems, Ms, other than strain = 0.7), and 8 (mature stems, strain = 0.7). Different letters indicate statistical differences (Tukey's HSD test, family-wise error rate = 0.05). (B) Ratio of the PD extension of the axial organs in *D. paniculatum* when the applied strain is 0.5. (C) Ratio of the PD extension of axial organs in three other species when the applied strain is 0.5. N = 15 (*P. vulgaris* petioles), 16 (*P. vulgaris* pulvini), 12 (*V. angularis*), and 11 (*V. unguiculata*). $^{***}p < 0.001$ by two-sided Welch's *t*-test. The calculated t-statistics for *P. vulgaris*, *V. angularis*, and *V. unguiculata* are 12.20, 9.04, and 9.05, respectively. (D) Serial images of side views of *D. paniculatum* pulvini during compression with a creep meter.

Table 1. The amount of cell-wall components (μg/gAIR) in aerial axial organs

	Primary pulvinus			Secondary pulvinus			Petiole			Developing stem			Mature stem		
	Mean	SD		Mean	SD		Mean	SD		Mean	SD		Mean	SD	
Glc***	228.97	8.27	ab	180.03	5.46	a	345.59	20.16	bc	221.73	15.08	ab	401.62	19.84	c
GalA***	157.30	5.98	a	126.41	8.79	ab	109.45	6.01	abc	96.89	4.89	bc	66.94	10.33	c
Xyl***	51.73	9.12	ab	33.49	3.43	a	108.06	8.60	b	30.05	1.65	a	143.79	10.76	b
Gal***	46.61	1.73	ab	41.87	3.17	abc	30.51	3.02	bc	61.40	1.66	a	20.64	2.59	c
Man***	41.92	1.97	ab	39.57	1.49	abc	34.40	1.73	bc	43.92	1.06	a	30.57	2.76	c
Ara***	38.03	1.67	a	23.29	2.09	ab	21.58	1.82	bc	27.84	0.76	ac	16.25	1.77	b
Rha***	14.08	0.34	a	11.17	0.92	ab	10.25	0.67	bc	12.03	0.14	ac	8.13	0.99	b
GlcA***	2.86	0.18	a	2.17	0.18	ab	2.51	0.28	ab	2.67	0.12	a	2.04	0.17	b
Fuc***	2.88	0.29	a	2.41	0.12	ab	2.14	0.26	bc	2.52	0.23	ac	1.33	0.15	b
Total***	584.37	15.82	ab	460.40	17.74	a	664.48	30.48	b	499.05	23.41	a	691.31	36.70	b

n = 6; ***$p < 0.001$ by the Kruskal-Wallis H-test; a-c, different characters indicate significantly different ($p<0.05$) by pairwise test for multiple comparisons of mean rank sums (Dunn's test; Holm's method)